Separation Science and Technology
Publication details, including instructions for authors and subscription information:
http://www.informaworld.com/smpp/title~content=t713708471

Effect of particle-size and pore-size distributions in cross-flow filtration

Stuart H. Munson-McGee[a]
[a] Department of Chemical Engineering, New Mexico State University, Las Cruces, New Mexico, U.S.A.

Online publication date: 23 April 2002

To cite this Article Munson-McGee, Stuart H.(2002) 'Effect of particle-size and pore-size distributions in cross-flow filtration', Separation Science and Technology, 37: 3, 493 — 513
To link to this Article: DOI: 10.1081/SS-120001444
URL: http://dx.doi.org/10.1081/SS-120001444

SEPARATION SCIENCE AND TECHNOLOGY, 37(3), 493–513 (2002)

EFFECT OF PARTICLE-SIZE AND PORE-SIZE DISTRIBUTIONS IN CROSS-FLOW FILTRATION

Stuart H. Munson-McGee

Department of Chemical Engineering, New Mexico State University, Las Cruces, New Mexico 88003

ABSTRACT

This paper presents the results of a finite-element model of cross-flow filtration that examines both radial and axial variations in velocity and concentration for different particle-size and pore-size distributions modeled using a lognormal distribution function. Also examined was the roll of particle diffusion. Assuming that the properties of the fluid were independent of the particle concentration allowed the Navier–Stokes equations to be solved independently from the mass transport problem. Flow at an inlet Reynolds number of 2000 was examined at constant inlet pressure and pressure outside the membrane. Once the velocity profiles had been determined, concentration profiles and permeate concentration were calculated for monodisperse particles as a function of pore-size distribution. The permeate concentrations were then numerically integrated to determine the permeate concentration of polydisperse particles. These results demonstrate that a six-order-of-magnitude reduction in the particulate concentration in the permeate can only be achieved when both the pore-size and particle-size distributions are narrow. Furthermore, they provide guidance for the average pore size necessary to achieve a specified

level of purity in the permeate depending on the particle-size distribution and operating conditions of the filtration unit.

INTRODUCTION

Ultrafiltration is a physical separation process that can remove particles as small as 0.001 μm (1). Typically, the process consists of hollow, semi-permeable fibers with the liquid containing the suspended particles flowing through the inner portion of the fibers. A differential pressure across the fiber wall causes the fluid to flow through the membrane. As the fluid passes through the wall, the particulate matter is separated from the liquid. The "purified" liquid is referred to as the permeate while the stream in which the particles has been concentrated is referred to as the retentate.

This rather simple physical process has received attention from experimentalists as well as theoreticians. The experimental work has reported the effectiveness of ultrafiltration on a variety of systems [see, for example, the review by Porter (2)]. In general, these reports demonstrate that ultrafiltration is a commercially viable separation process. However, care must be taken in selecting the components and the operating conditions, especially with regards to backwashing or other techniques (3,4) to minimize performance degradation caused by fouling of the membrane surfaces by the contaminants.

Theoretical modeling has focused generally in the following areas: membrane fouling, filtration efficiency, and process simulation. A great deal of work has been done in the area of membrane fouling [see, for example, the review by Fane and Fell (5)]. Three fouling mechanisms have been identified (6), surface pore blocking, plugging within the pore, and surface fouling (i.e., gel layer or cake formation). Most of the attention has been paid to surface fouling which decreases the permeate flux and can also decrease the concentration of the contaminant in the permeate by creating effectively smaller pores in the membrane. The principle mechanism for cake formation is particles adhering to the membrane surface due to either fluid or electrostatic forces. Force balance analyses (7–12) have been used to describe transient cake formation and can account for particle size distributions within the cake (smaller particles are deposited nearest to the original membrane surface). Other analyses have included gel layer formation (13,14), colloidal interaction (15), mass transfer kinetics (16,17), and neural networks (18–20).

Modeling the efficiency of the ultrafiltration process has focused on determining the role of the particle-size distribution and the pore-size distribution (10,21,22). These analyses have limited themselves to examining

MARCEL DEKKER, INC.
270 Madison Avenue, New York, New York 10016

only a differential length of the ultrafiltration membrane or, equivalently, have assumed that the pressure, velocity, and concentration in the filtration tube were not a function of axial position. And although permeate concentration was one aspect of this research, cake formation was also a significant portion of the analyses.

Simulating the entire ultrafiltration process has also received some attention (23,24). These models have examined the performance of single units as well as multiple unit schemes and relied on experimentally determined relationships to relate operating conditions, particle size, and membrane properties to the permeate flux and concentration.

In a companion project to this one, the ultrafiltration process was examined for its potential to remove trace heavy-metal contaminants from an aqueous stream. To enhance the filtration rate, pretreatment of the feed stream was necessary. To aid in that study, a theoretical model of the process was developed which included axial and radial variations in the velocity and concentration profiles. In this model, the effects of both the pore-size distribution and the particle-size distribution on the efficiency of the ultrafiltration process were examined. In addition, the effects of flow rate at constant inlet pressure and the diffusivity of the particles were also examined. Since the model assumed steady state operation, the effect of cake formation was not addressed. In the remainder of this paper, the model formulation is presented and results for selected conditions presented. Finally, contaminant concentration in the permeate as a function of pore and initial contaminant size distributions are presented.

THEORETICAL MODEL DEVELOPMENT

The cross-flow filtration apparatus modeled in this work was a cylindrical tube with a porous membrane surface. It was assumed that the flow was radially symmetric, that body forces could be neglected, that both the viscosity and density were constant, and that steady state had been reached. The geometry of the model was described the length of the permeable-wall section, L, and the internal radius, R.

Fluid Dynamics

The momentum conservation equation for the simplified flow described above is the well known Navier–Stokes equation and is given in vector form by

$$\rho(\mathbf{v}\cdot\nabla)\cdot\mathbf{v} + \nabla P - \eta\nabla^2\mathbf{v} = 0 \tag{1}$$

MARCEL DEKKER, INC.
270 Madison Avenue, New York, New York 10016

For the cylindrical geometry of interest here, the radial and axial components of the Navier–Stokes equation become (25)

$$\rho\left(v_r\frac{\partial v_r}{\partial r}+v_z\frac{\partial v_r}{\partial z}\right)=-\frac{\partial P}{\partial r}+\eta\left[\frac{\partial}{\partial r}\left(\frac{1}{r}\frac{\partial(rv_r)}{\partial r}\right)+\frac{\partial^2 v_r}{\partial z^2}\right] \tag{2}$$

$$\rho\left(v_r\frac{\partial v_z}{\partial r}+v_z\frac{\partial v_z}{\partial z}\right)=-\frac{\partial P}{\partial z}+\eta\left[\frac{1}{r}\frac{\partial}{\partial r}\left(r\frac{\partial v_z}{\partial r}\right)+\frac{\partial^2 v_z}{\partial z^2}\right] \tag{3}$$

where r and z are the radial and axial directions, v_r and v_z the velocity components in the r and z directions, P the pressure, ρ the density, and η the viscosity. To facilitate numerical solution of these expressions, the following dimensionless variables were introduced.

$$\hat{r}=\frac{r}{R} \tag{4}$$

$$\hat{z}=\frac{z}{L} \tag{5}$$

$$\hat{v}_r=\frac{v_r}{v_r^*} \tag{6}$$

$$\hat{v}_z=\frac{v_z}{v_z^*} \tag{7}$$

The velocity scaling variables were chosen so that the maximum dimensionless velocities would be approximately one. These velocities, chosen to be the anticipated maximum flow rate through the membrane wall and the centerline velocity at the inlet, are given by

$$v_r^*=k(P_0-P_{\text{atm}}) \tag{8}$$

$$v_z^*=\frac{\eta}{\varrho R}N_{Re} \tag{9}$$

where k is the membrane permeability, P_0 and P_{atm} are the pressures at the inlet to the unit and on the permeate side of the membrane, and N_{Re} is the Reynolds number. Equation (8) represents a Darcy's law type flow through the membrane.

MARCEL DEKKER, INC.
270 Madison Avenue, New York, New York 10016

Substituting Eqs. (4)–(7) into Eqs. (2) and (3), expanding the derivatives, and rearranging the results provided the following expressions

$$\rho\hat{r}^2\left[\frac{\left(v_r^*\right)^2}{R}\hat{v}_r\frac{\partial\hat{v}_r}{\partial\hat{r}}+\frac{v_r^*v_z^*}{L}\hat{v}_z\frac{\partial\hat{v}_r}{\partial\hat{z}}\right]$$
$$=-\frac{\hat{r}^2}{R}\frac{\partial P}{\partial\hat{r}}+\eta\left\{\frac{v_r^*}{R^2}\left[\hat{r}\frac{\partial^2(\hat{r}\hat{v}_r)}{\partial\hat{r}^2}-\frac{\partial(\hat{r}\hat{v}_r)}{\partial\hat{r}}\right]+\frac{v_r^*}{L^2}\hat{r}^2\frac{\partial^2\hat{v}_r}{\partial\hat{z}^2}\right\} \tag{10}$$

$$\rho\hat{r}\left[\frac{v_r^*v_z^*}{R}\hat{v}_r\frac{\partial\hat{v}_z}{\partial\hat{r}}+\frac{\left(v_z^*\right)^2}{L}\hat{v}_z\frac{\partial\hat{v}_z}{\partial\hat{z}}\right]$$
$$=-\frac{\hat{r}}{L}\frac{\partial P}{\partial\hat{z}}+\eta\left\{\frac{v_z^*}{R^2}\left[\frac{\partial\hat{v}_z}{\partial\hat{r}}+\hat{r}\frac{\partial^2\hat{v}_z}{\partial\hat{r}^2}\right]+\frac{v_z^*}{L^2}\hat{r}\frac{\partial^2\hat{v}_z}{\partial\hat{z}^2}\right\} \tag{11}$$

The equation describing the pressure variation within the unit was derived by using the divergence operator on the Navier–Stokes equations and applying the conservation of mass to eliminate terms. The final expression is given in vector form as (26)

$$\nabla^2P+\rho\nabla\cdot[(\mathbf{v}\cdot\nabla)\cdot\mathbf{v}]=0 \tag{12}$$

and in cylindrical coordinates as

$$\frac{1}{r}\frac{\partial}{\partial r}\left(r\frac{\partial P}{\partial r}\right)+\frac{\partial^2P}{\partial z^2}+2\rho\left(\frac{\partial v_r}{\partial r}\frac{\partial v_z}{\partial z}-\frac{\partial v_r}{\partial z}\frac{\partial v_z}{\partial r}\right)=0 \tag{13}$$

To ensure that the continuity equation, given in cylindrical coordinates as

$$\frac{1}{r}\frac{\partial(rv_r)}{\partial r}+\frac{\partial v_z}{\partial z}=0 \tag{14}$$

was also satisfied, it was multiplied by an arbitrary weighting factor and added to Eq. (13). Using the dimensionless variables above, the final expression became

$$\left(\frac{L}{R}\right)^2\left(\frac{\partial P}{\partial\hat{r}}+\hat{r}\frac{\partial^2P}{\partial\hat{r}^2}\right)+\hat{r}\frac{\partial^2P}{\partial\hat{z}^2}-\hat{r}\left(2\rho\frac{L}{R}\right)\left(\frac{v_r^*}{v_z^*}\right)\left[\frac{\partial\hat{v}_r}{\partial\hat{r}}\frac{\partial\hat{v}_z}{\partial\hat{z}}-\frac{\partial\hat{v}_r}{\partial\hat{z}}\frac{\partial\hat{v}_z}{\partial\hat{r}}\right]$$
$$+w\left[\frac{v_r^*}{R}\frac{\partial(\hat{r}\hat{v}_r)}{\partial\hat{r}}+\hat{r}\frac{v_z^*}{L}\frac{\partial\hat{v}_z}{\partial\hat{z}}\right]=0 \tag{15}$$

where w is the weighting factor to ensure that the continuity equation is satisfied.

Mass Transport

In cylindrical coordinates, the relevant form of the continuity equation is given by

$$v_r \frac{\partial C_i}{\partial r} + v_z \frac{\partial C_i}{\partial z} = D\left[\frac{1}{r}\frac{\partial}{\partial r}\left(r\frac{\partial C_i}{\partial r}\right) + \frac{\partial^2 C_i}{\partial z^2}\right] \tag{16}$$

where D is the diffusivity and C_i is the concentration of the ith species. Expressed in terms of the dimensionless variables, Eq. (16) becomes

$$\hat{v}_r \frac{v_r^*}{R}\frac{\partial C_i}{\partial \hat{r}} + \hat{v}_z \frac{v_z^*}{L}\frac{\partial C_i}{\partial \hat{z}} = D\left[\frac{1}{R^2}\left(\frac{1}{\hat{r}}\frac{\partial C}{\partial \hat{r}} + \frac{\partial^2 C_i}{\partial \hat{r}^2}\right) + \frac{1}{L^2}\frac{\partial^2 C_i}{\partial \hat{z}^2}\right] \tag{17}$$

The concentration in the permeate and adjacent to the inside membrane surface can be related to one another using sieving analysis (7,27,28). These analyses are developed in terms of both particle-size distributions and pore-size distributions. A variety of distribution shapes have been measured for pore-size distributions (29) and recently (30) the errors in prior use of the lognormal distribution function have been identified and corrected. The lognormal distribution is used in this work for the pore-size distribution and is given by

$$n(r_p) = \frac{1}{2\sqrt{\sigma}} e^{(\log_{10}(r_p) - \log_{10}(\mu))/2\sigma^2} \tag{18}$$

where r_p is the pore radius and μ and σ are the mean and standard deviation of the distribution and are given by

$$\mu = \int_0^\infty r_p\, n(r_p)\, dr_p \tag{19}$$

and

$$\sigma = \int_0^\infty (r_p - \mu)^2\, n(r_p)\, dr_p \tag{20}$$

In Fig. 1, three distribution functions have been plotted that all have the same mean but different standard deviations. From this Figure we see that as the standard deviation increases, the radius at which the maximum in the distribution function occurs becomes smaller and the width of the distribution function increases.

MARCEL DEKKER, INC.
270 Madison Avenue, New York, New York 10016

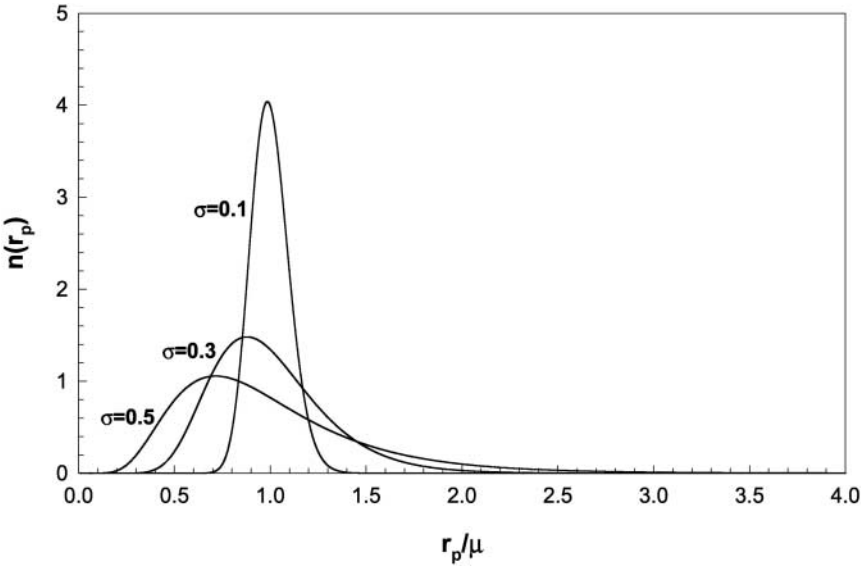

Figure 1. Lognormal distributions for $\mu = 1$ and $\sigma = 0.1, 0.3$, and 0.5.

The relationship between the permeate and the inside membrane surface concentrations is given by (27)

$$C_{ip} = s\, C_i \tag{21}$$

where s is the sieving coefficient, which is a function of both the pore-radius distribution, $n(r_p)$, and the contaminant particle size, r_c, and is given by

$$s(r_c) = \frac{\int_0^\infty q(r_p) F(r_p, r_c)\, dr_p}{\int_0^\infty q(r_p)\{1 + F(r_p, r_c) e^{-\mathrm{Pe}(r_p)}\}\, dr_p} \tag{22}$$

The functions in Eq. (22) (i.e., $q(r_p)$, $F(r_p,r_c)$ and $\mathrm{Pe}(r_p)$) are given in the original reference. In the current work, the normalizing dimension x_0 is the mean of the pore radii rather than the smallest particle of interest. It is important to note that in this formulation, the sieving coefficient is a function of the transmembrane pressure through both $F(r_p, r_c)$ and $\mathrm{Pe}(r_p)$.

Typical dependence of the sieving coefficient on the particle size and transmembrane pressure for assumed pore-radius distribution parameters of $\mu = 1.0$ and $\sigma = 0.3$ is shown in Fig. 2 where a dimensionless transmembrane

MARCEL DEKKER, INC.
270 Madison Avenue, New York, New York 10016

pressure, T_0, has been introduced (26). This quantity is given by

$$T_0 = \frac{(P|_{r=R} - P_{\text{atm}})\mu^2}{16\eta\,\rho\,R} \tag{23}$$

where $P|_{r=R}$ is the pressure at the inside wall surface and is a function of axial distance and P_{atm} is the pressure outside of the membrane.

The curves in Fig. 2 have three distinct regions, at high values of T_0 they are constant and then increase to an asymptotic value of 1.0 at very low values of T_0. To actually evaluate the sieving coefficient within the finite element program, a table of sieving coefficients for each particle size as a function of transmembrane pressure and pore-radius distribution was constructed. This data was then approximated for each ratio r_c/μ using

$$s = \begin{cases} 1 & \text{for } \log_{10}(T_0) < a_\infty \\ a_0 + \dfrac{(1 - a_0)}{(1 + a_1 x + a_2 x^2 + a_3 x^4)^n} & \text{for } \log_{10}(T_0) \geq a_\infty \end{cases} \tag{24}$$

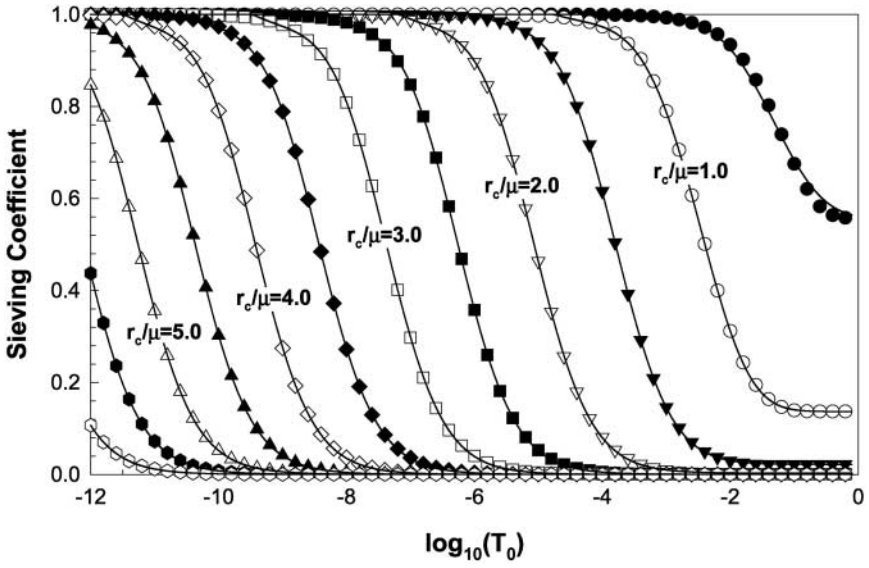

Figure 2. Sieving coefficient as a function of the transmembrane pressure and normalized contaminant particle radius for $\sigma = 0.3$ and $\mu = 1.0$. The symbols represent numerical solutions to Eq. (22) while the solid curves represent the least squares fit to the numerical solution using Eq. (24).

MARCEL DEKKER, INC.
270 Madison Avenue, New York, New York 10016

where

$$x = \log_{10}(T_0) - a_\infty \tag{25}$$

The six parameters (i.e., a_i and n) were determined using a nonlinear least squares technique that minimized sum of the square of the error at each point.

To find the concentration of the contaminant in the permeate, the following procedure was used. First, the normalized concentration was determined as a function of particle size, viz.

$$\frac{C_{ip}}{C_{i0}} = \frac{\int_0^L s\, v_r(z)\, C_i(z)\, dz}{\int_0^L v_r(z)\, dz} \tag{26}$$

where C_{ip}, C_{i0}, and C_i are the concentration of the i-th size particle in the permeate, in the input, and at the inside membrane surface.

Recognizing that C_{i0} can be related to the input concentration, C_0, through the contaminant particle size distribution, $n(r_c)$, viz.

$$C_{i0} = n(r_c)\, C_0 \tag{27}$$

the normalized concentration in the permeate can be found from

$$\frac{C_p}{C_0} = \int_0^\infty n(r_c)\, \frac{C_{ip}}{C_{i0}}\, dr \tag{28}$$

The contaminant particle size was also assumed to follow a lognormal probability density distribution with a mean and standard deviation given by μ_c and σ_c, respectively.

To reduce the computational burden, Eq. (26) was evaluated for particle sizes ranging from $0 \le r_c/\mu \le 10$ as a function of the operating conditions (i.e., N_{Re}, P_0, P_{atm}, and k) for a unit input concentration. These results were weighted by the contaminant particle size distribution and then numerically integrated using Simpson's rule to determine the concentration in the permeate. This was done for a variety of contaminant distributions.

Boundary Conditions

The velocity profile at the inlet to the unit was assumed to be fully developed, the concentration to be uniform, and the pressure to be known. The boundary conditions at this location were specified as:

$$\hat{v}_r = 0; \quad \hat{v}_z = 1 - \hat{r}^2; \quad P = P_0; \quad C_i = C_0 \tag{29}$$

MARCEL DEKKER, INC.
270 Madison Avenue, New York, New York 10016

Along the centerline (i.e., at $\hat{r} = 0$), symmetry was assumed and the boundary conditions were given by:

$$\hat{v}_r = \frac{\partial \hat{v}_z}{\partial r} = \frac{\partial P}{\partial r} = \frac{\partial C_{\mathrm{i}}}{\partial r} = 0 \tag{30}$$

At the exit from the filtration unit, the gradients were specified to be zero, viz.

$$\frac{\partial \hat{v}_r}{\partial z} = \frac{\partial \hat{v}_z}{\partial z} = \frac{\partial P}{\partial z} = \frac{\partial C_{\mathrm{i}}}{\partial z} = 0 \tag{31}$$

The most difficult boundary condition to specify was along the surface of the unit (i.e., at $\hat{r} = 1$). The radial velocity was assumed to be given by Darcy's law at the membrane wall, i.e., Eq. (8). Nassehi (31) has discussed coupling the Navier–Stokes equations and Darcy's law. It was assumed that the no-slip condition applied to the axial velocity, i.e., $\hat{v}_z = 0$. The pressure boundary condition was derived (26) from the Navier–Stokes equations to satisfy the definition

$$\frac{\partial P}{\partial n} = \mathbf{n}\cdot\nabla P \tag{32}$$

where $\mathbf{n}$ is the outward normal at the boundary. In vector notation, this is given by

$$\frac{\partial P}{\partial n} = \eta \mathbf{n}\cdot\nabla^2\mathbf{v} - \rho\mathbf{n}\cdot[(\mathbf{v}\cdot\nabla)\cdot\mathbf{v}] \tag{33}$$

In cylindrical coordinates when applied to a boundary at constant radius (i.e., when $n_z = 0$), it is given as (26)

$$\frac{\partial P}{\partial r} = n_r\left[\eta\left(\frac{1}{r}\frac{\partial}{\partial r}r\frac{\partial v_r}{\partial r} - \frac{v_r}{r^2} + \frac{\partial^2 v_r}{\partial z^2}\right) - \rho\left(v_r\frac{\partial v_r}{\partial r} + v_z\frac{\partial v_r}{\partial z}\right)\right] \tag{34}$$

Introducing the dimensionless variables, applying the no-slip boundary condition, and expanding the derivatives, Eq. (34) becomes

$$\frac{\partial P}{\partial \hat{r}} = n_r\left\{\frac{\eta v_r^*}{R}\left[\frac{\partial^2 \hat{v}_r}{\partial \hat{r}^2} + \frac{1}{\hat{r}}\frac{\partial \hat{v}_r}{\partial \hat{r}} - \frac{\hat{v}_r}{\hat{r}^2} + \left(\frac{R}{L}\right)^2\frac{\partial^2 \hat{v}_r}{\partial \hat{z}^2}\right] - \rho\left(v_r^*\right)^2\hat{v}_r\frac{\partial \hat{v}_r}{\partial \hat{r}}\right\} \tag{35}$$

Finally, the concentration boundary condition was specified as (32).

$$\frac{\partial C_{\mathrm{i}}}{\partial r} = -\frac{v_r(C_{\mathrm{i}} - C_{\mathrm{pi}})}{D} \tag{36}$$

where C_{pi} is the concentration in the permeate. The final form of the boundary

MARCEL DEKKER, INC.
270 Madison Avenue, New York, New York 10016

condition along the porous membrane surface for the concentration was

$$\frac{\partial C_{\mathrm{i}}}{\partial \hat{\mathrm{r}}} = \left(\frac{v_r^* R}{D}\right)(1-s)\hat{v}_r C_{\mathrm{i}} \tag{37}$$

Solution Procedure

Several approximate solutions for the fluid dynamics portion of this problem and similar problems have been given in Ref. (33–38). However, as discussed below, a finite element analysis was used in this work. For typical operation of the membrane units under consideration, nominal values were used for the model parameters (Table 1). The finite element grid was constructed with $0 \le \hat{r} \le 1.0$ and $0 \le \hat{z} \le 1.0$. The partial differential equations, along with the associated boundary conditions, were solved using commercial finite element software (39). The velocity and pressure distributions were determined using the following initial conditions:

$$v_z = 2\bar{v}_z\left(1-\hat{r}^2\right) \tag{38}$$

$$v_r = k\left[(a - P_{\mathrm{atm}}) + bz + cz^2\right]\left[2\hat{r} - \hat{r}^3\right] \tag{39}$$

$$P = a + bz + cz^2 \tag{40}$$

where $\bar{v}_z$ is the average axial velocity at any axial location and is given by

$$\bar{v}_z = \frac{N_{\mathrm{Re}}\eta}{2R\varrho} - \frac{2k}{R}\left[(a - P_{\mathrm{atm}})z + \frac{bz^2}{2} + \frac{cz^3}{3}\right] \tag{41}$$

Table 1. List of Parameter Values Used in the Simulations

Parameter	Symbol	Value
Internal radius	R	0.05 cm
Length	L	35 cm
Permeability	K	10^{-7} gm/cm^2 sec
Permeate pressure	P_{atm}	1.0×10^6 dynes/cm^2
Viscosity	η	10^{-2} gm/cm sec
Density	ρ	1.0 gm/cm^3
Diffusivity	D	0.005–0.05 cm^2/s

The parameters a, b, and c are given by

$$a = P_{\text{in}} \tag{42}$$

$$b = -\frac{4\eta^2 N_{\text{Re}}}{\rho R^3} \tag{43}$$

$$c = 24\frac{\eta k}{\rho R^3} \times \frac{(P_{\text{in}} - P_{\text{atm}})\rho R^3 - 2\eta^2 L N_{\text{Re}}}{3R^3 - 8\eta k L^2} \tag{44}$$

where P_{in} and P_{atm} are the pressures at the inlet to the unit and on the permeate side of the unit, respectively.

The initial conditions were derived (40) based on the assumptions that:

1. the pressure variation along the length of the unit could be approximated by a quadratic polynomial and
2. the axial velocity could be approximately given by a modified form of the Hagen–Poiseuille result (36).

Application of conservation of mass resulted in the approximations given above.

Once the velocity and pressure distributions had been calculated, the values on a 101 point by 101 point grid were stored for subsequent use. The concentration profiles were found using a separate finite element program (which read the stored velocity values and interpolated these values at the node points as needed) for a variety of pore-size distributions.

RESULTS

In the model formulated above, the velocity profiles are independent of the contaminant concentration since the density and viscosity were assumed to be constant. Therefore, we can examine the effects of the operating parameters on the velocity fields and then use these results to determine the concentration profiles and, ultimately, the concentration of the contaminant in the permeate stream.

Fluid Dynamics

The axial velocity profiles characteristically demonstrated a monotonic decrease along the centerline as material was withdrawn from the unit through the permeable wall (Fig. 3) for the case $N_{\text{Re}} = 2000$ and $P_{\text{in}} = 2.0 \times 10^6$ dynes/cm^2 (other parameters are given in Table 1). The magnitude of this decrease depended upon the Reynolds number and the radial driving force given by the product of the permeability and the pressure difference between the inside and outside of the

MARCEL DEKKER, INC.
270 Madison Avenue, New York, New York 10016

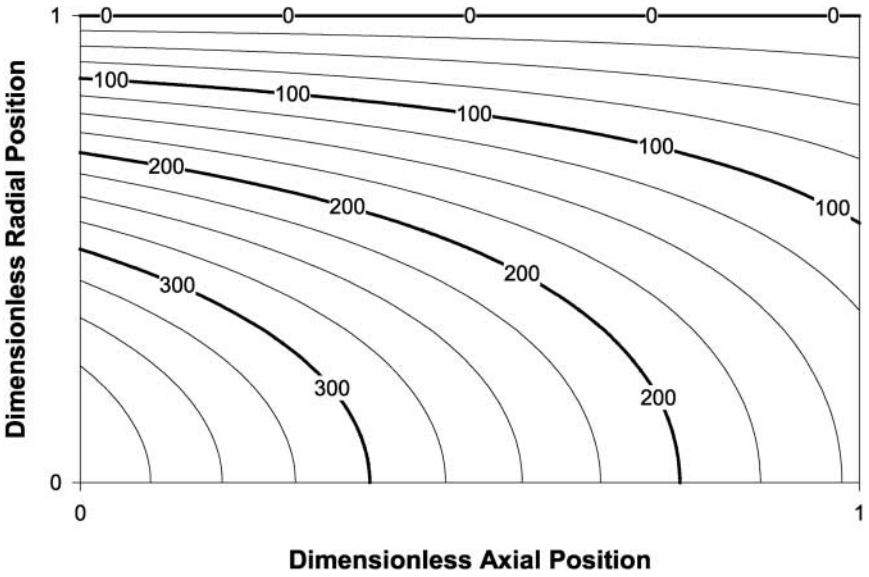

Figure 3. Axial velocity contours for $N_{Re} = 2000$ and $P_{in} = 1.25 \times 10^6$ dynes/cm^2.

unit. The higher the Reynolds number or the smaller the radial driving force, the smaller the relative decrease in the centerline axial velocity.

The radial velocity (Fig. 4) has the same qualitative shape as those derived by Middleman (36) for similar flow conditions. As expected, the radial velocity at the centerline is zero while it remains finite at the porous wall with the magnitude at the porous wall being proportional to the difference in pressure between the inside and outside of the filtration unit. Also as expected from the momentum conservation equation, there is a maximum in the radial velocity at $\hat{r} = 2/3$, which is consistent with prior results (36) (when the typographical errors in that work are corrected).

The magnitude of the pressure gradient along the filtration unit (Fig. 5) slowly decreases with axial position as the fluid is removed from the unit. The decrease is qualitatively similar to prior results (36) in which an exponential decay was derived. The difference between the quadratic decay used as the initial condition approximation and the exponential decay will be discussed further elsewhere (40).

Concentration Profiles

Concentration profiles were determined for a variety of monodisperse particle sizes at two diffusivities ($D = 0.005$ gm/cm^2 sec and 0.05 gm/cm^2 sec)

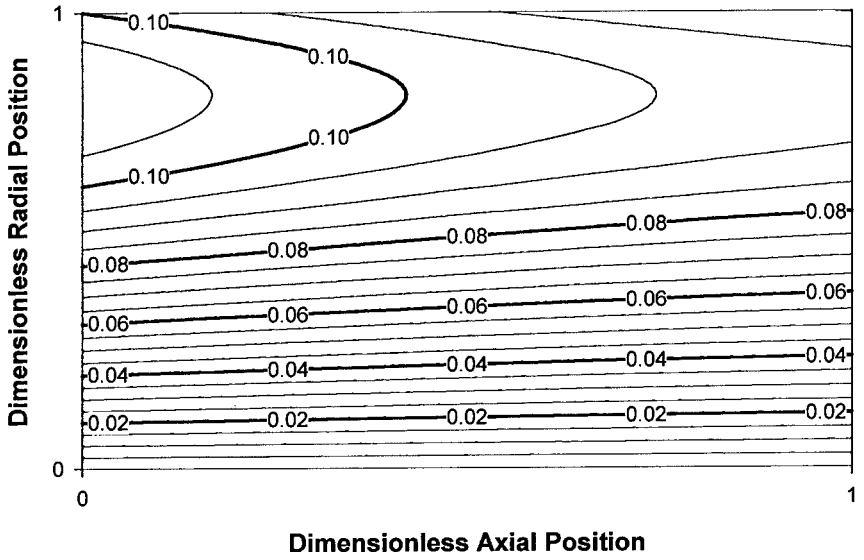

Figure 4. Radial velocity contours for flow conditions as in Fig. 3.

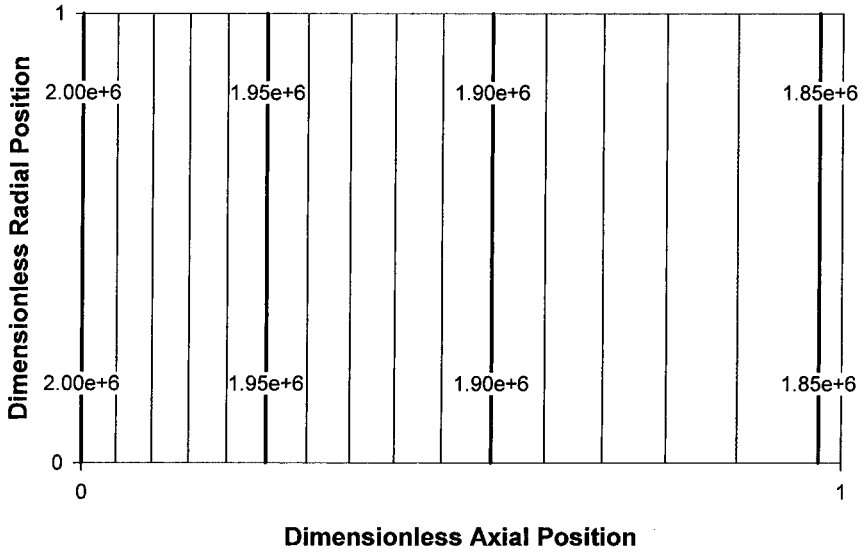

Figure 5. Pressure contours for flow conditions as in Fig. 3.

MARCEL DEKKER, INC.
270 Madison Avenue, New York, New York 10016

and three pore-size distribution breadths ($\sigma = 0.1, 0.3$, and 0.5). Depending on the breadth of the pore-size distribution, these profiles were determined for particles sizes that ranged from $r_c/\mu = 0.05$ to 2.0 or as great as 10.0 in 0.05 increments. Illustrative results (Fig. 6) show that increasing the pore-size distribution (i.e., going down in either column in Fig. 6) causes the maximum concentration to decrease but leaves the qualitative shape of the curves unchanged. This reflects the fact that as the pore-size distribution becomes broader there are more large pores through which more of the contaminant can pass.

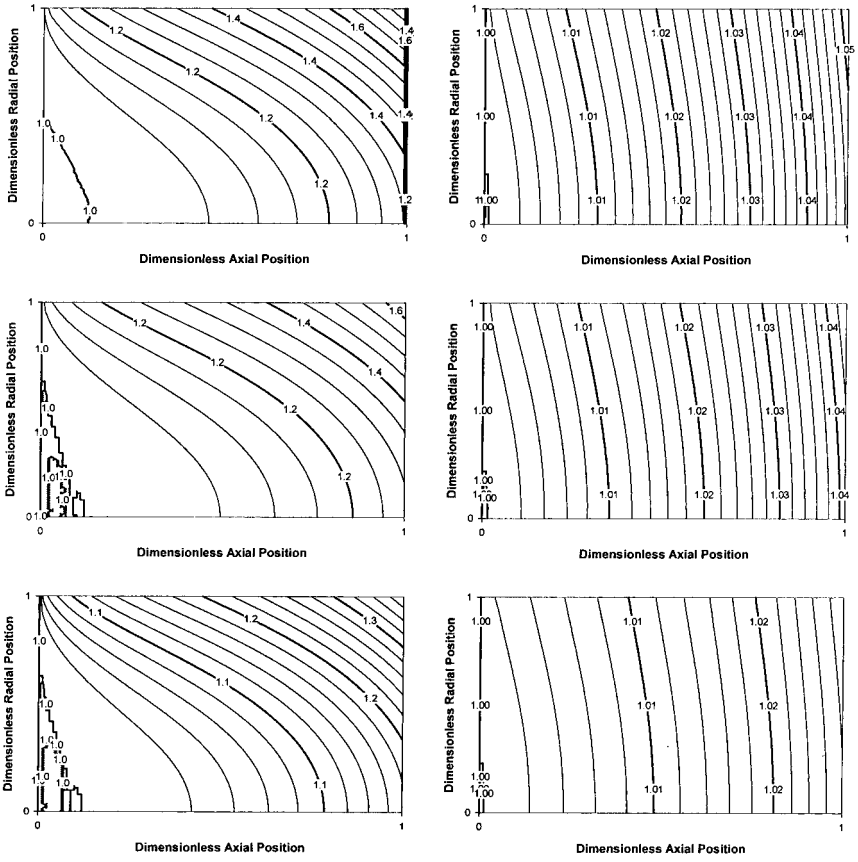

Figure 6. Concentration contours for $r_c/\mu = 1.0$. The columns correspond to constant diffusivities ($D = 0.005$ and $0.05\,\text{gm/cm}^2\,\text{sec}$; left to right). The rows correspond to constant breadth of the pore-size distribution ($\sigma = 0.1, 0.3$, and 0.5; top to bottom). Other flow conditions as in Fig. 3.

Comparing the columns in Fig. 6 shows the effect of the diffusivity at constant pore-size distribution. As the diffusivity increases, the rate at which the particles diffusive away from the porous wall increases and the concentration profiles become flatter. For a given pore-size distribution, this also manifests itself in lower average concentrations and lower concentrations adjacent to the porous wall. As discussed below, this will have a slight effect on the permeate concentration too.

Permeate Concentration

Permeate concentrations were determined for a variety of monodispersed particles as a function of the standard deviation of the pore-radius distribution (σ) at two different diffusivities (D) for the base case of $N_{Re} = 2000$ and $P_{\text{in}} = 1.25 \times 10^6$ dynes/cm^2 (Fig. 7). When the breadth of the pore-size distribution was narrow, particle diffusivity had little effect on the calculated permeate concentration. Furthermore, when the particle was approximately 1.5 times the average pore radius, a six-order-of-magnitude reduction in the contaminant

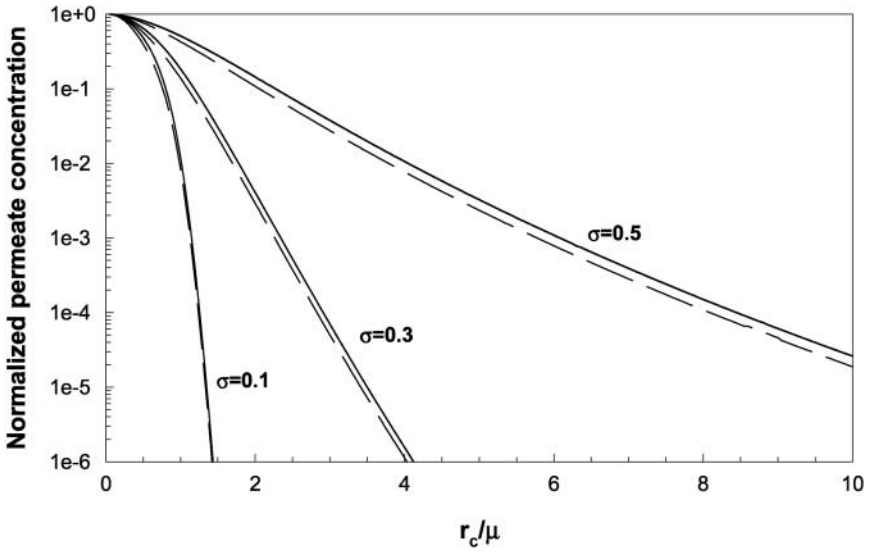

Figure 7. Normalized permeate concentrations for monodisperse particles as a function of normalized particle radius and the breadth of the pore-size distribution. The solid lines correspond to a diffusivity of 0.05 cm^2/s and the dashed lines correspond to a diffusivity of 0.005 cm^2/s.

concentration was achieved. As the breadth of the pore-size distribution increased, the effect of the diffusivity increased with a higher diffusivity leading to lower permeate concentration. Also, as the pore-size distribution became broader, it became more difficult to achieve a six-order-of-magnitude reduction. For the case of $\sigma = 0.3$, the particle size must be nearly four times as large as the average pore size to accomplish this level of purification. When $\sigma = 0.5$, a particle ten times larger than the average pore size leads to only a four to five-order-of-magnitude reduction in the purity of the permeate.

When a distribution of contaminant particle sizes was included in the analysis the separation process became more inefficient (Fig. 8). For narrow distributions of both pore and particle sizes, a six-order-of-magnitude reduction could still be accomplished when the average particle size was approximately twice the average pore radius compared to approximately 1.5 times with monodisperse particles. As the distributions become broader, the level of purification decreases quickly. For example, when the average particle size was twice the average pore size, the permeate concentration was about two orders of magnitude less than in input concentration for $\sigma = 0.3$, while it was only about one-half the input concentration when $\sigma = 0.5$. For the latter case, even an

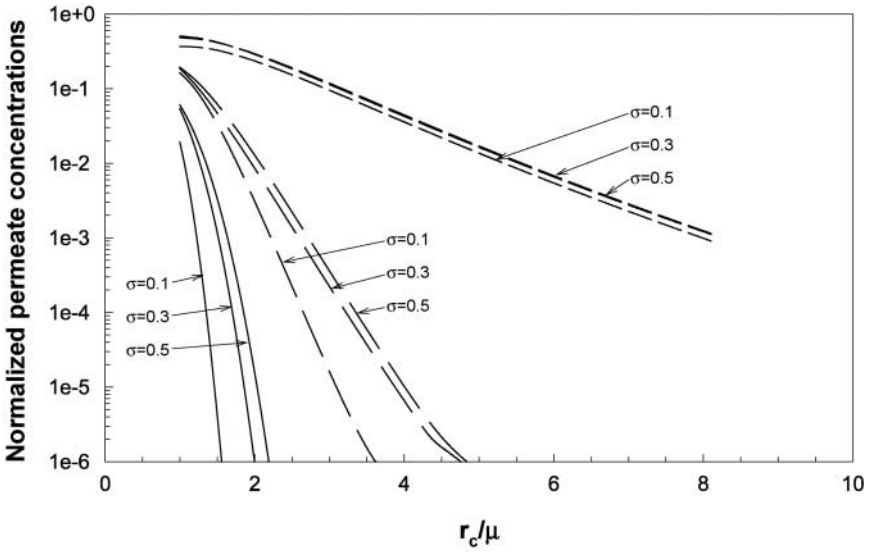

Figure 8. Normalized permeate concentrations for polydisperse particles as a function of normalized particle radius, the breadth of the pore-size distribution, and the breadth of the particle size distribution for $D = 0.005\,\mathrm{cm}^2/\mathrm{s}$. The solid lines correspond to $\sigma_c = 0.1$, the long dashed lines to $\sigma_c = 0.3$, and the short dashed lines to $\sigma_c = -0.5$, respectively.

average particle radius an order of magnitude larger than the average pore radius resulted in a three-order-of-magnitude reduction in the permeate concentration.

From these results, the necessity of having a narrow pore-size distribution is apparent if high purity levels are to be obtained. When the pore distribution is broad, there are a sufficient number of large pores and small particles that the concentration in the permeate can not be sufficiently reduced even if an average pore size that is one tenth of the average particle size is used.

SUMMARY AND CONCLUSIONS

In this work the following process was used to calculate the contaminant concentration in the permeate of a cross-flow filtration unit:

- Determine the pressure, axial velocity, and radial velocity profiles for a given set of operating conditions by solving the Navier–Stokes equations using a finite element analysis,
- Determine the concentration profiles for monodisperse particles by solving the continuity equation in conjunction with sieving analysis and the membrane pore-size distribution for various particle sizes using finite element analysis,
- Determine the normalized concentrations for each size particle in the permeate, and
- Determine the normalized contaminant concentration in the permeate by weighting the individual particle size concentrations by the initial particle size distribution.

For monodisperse particles, it was demonstrated that the pore-radius distribution had a significant effect on the concentration profiles within the filtration unit and the permeate concentration. It was also shown that the particle diffusivity effected the efficiency of the filtration unit with the higher the diffusivity the higher the unit's efficiency. The best performance in terms of the lowest concentration of contaminant in the permeate was obtained with narrow pore distributions and high values of the diffusivity.

For polydisperse particles, it was demonstrated that breadth of both the pore-radius and particle-radius distributions effected the permeate concentrations. With narrow distributions, a six-order-of-magnitude reduction in concentration could be obtained when the mean particle radius was twice the mean pore radius. However, as the distributions became broader, a mean particle radius that was four times the mean pore radius would result in only a single-order-of-magnitude reduction in the concentration. The degradation in performance occurred more quickly as the breadth of the pore-radius distribution increased than when the particle-radius distribution increased.

MARCEL DEKKER, INC.
270 Madison Avenue, New York, New York 10016

ACKNOWLEDGMENTS

The author is grateful to Dr. Keith Fife of the Actinide Process Chemistry Group in the Nuclear Materials Technology Division at the Los Alamos National Laboratory for both suggesting this problem to him as well as providing the means to accomplish it.

REFERENCES

1. Miller, S.A.; et al. Liquid–Solid Systems. In *Perry's Chemical Engineer's Handbook*, 6th Ed. Perry, R.H., Chilton, C.H., Eds., McGraw-Hill: New York, 1984, 19–97.
2. Porter, M.C. Membrane Filtration. In *Handbook of Separation Techniques for Chemical Engineers*, 3rd Ed. Schweitzer, P.A. Ed.; McGraw–Hill: New York, 1996; 78–83.
3. Robinson, C.W.; Siegel, M.H.; Condemine, A.; Fee, C.; Fahidy, T.Z.; Glick, B.R. Pulsed-Electric-Field Crossflow Ultrafiltration of Bovine Serum Albumin. J. Membr. Sci. **1993**, *80*, 209–220.
4. Arroyo, G.; Fonade, C. Use of Intermittent Jets to Enhance Flux in Crossflow Filtration. J. Membr. Sci. **1993**, *80*, 117–129.
5. Fane, A.G.; Fell, C.J.D. A Review of Fouling and Fouling Control in Ultrafiltration. Desalination **1987**, *62*, 117–136.
6. Jonsson, G.; Pradanos, P.; Hernandez, A. Fouling Phenomena in Microporous Membranes. Flux Decline Kinetics and Structural Modifications. J. Membr. Sci. **1996**, *112*, 171–183.
7. Fillippov, A.; Starov, V.M.; Lloyd, D.R.; Chakravarti, S.; Glaser, S. Sieve Mechanism of Microfiltratiom. J. Membr. Sci. **1994**, *89*, 123–199.
8. Wang, W.; Jia, X.D.; Davies, G.A. A Theoretical Study of Transient Cross-Flow Filtration Using Force Balance Analysis. Chem. Engng J. **1995**, *60*, 55–62.
9. Fu, L.F.; Dempsey, B.A. Modeling the Effect of Particle Size and Charge on the Structure of the Filter Cake in Ultrafiltration. J. Membr. Sci. **1998**, *149*, 221–240.
10. Chang, D.-J.; Hwang, S.-J. Unsteady-State Permeate Flux of Cross Flow Microfiltration. Sep. Sci. Technol. **1994**, *29*, 1593–1608.
11. Hwang, S.-J.; Chang, D.-J.; Chen, C.H. Steady-State Permeate Flux for Particle Cross-Flow Filtration. Chem. Engng J. **1996**, *61*, 171–178.
12. Blake, N.J.; Cumming, I.W.; Streat, M. Prediction of Steady State Crossflow Filtration Using a Force Balance Model. J. Membr. Sci. **1992**, *68*, 205–216.

MARCEL DEKKER, INC.
270 Madison Avenue, New York, New York 10016

13. van Oers, C.W.; Vorstman, M.A.G.; II, W.G.; Muijselaar, M.; Kerkhof, P.J.A.M. Unsteady-State Flux Behavior in Relation to the Presence of a Gel Layer. J. Membr. Sci. **1992**, *73*, 231–246.
14. Field, R.W.; Aimar, P. Ideal Limiting Fluxes in Ultrafiltration: Comparison of Various Theoretical Relationships. J. Membr. Sci. **1993**, *80*, 107–115.
15. Bowen, W.R.; Mongruel, A.; Williams, P.M. Prediction of the Rate of Cross-Flow Membrane Ultrafiltration: A Colloidal Interaction Approach. Chem. Engng Sci. **1996**, *51* (18), 4321–4333.
16. Song, L. Flux Decline in Crossflow Microfiltration and Ultrafiltration: Mechanism and Modeling of Membrane Fouling. J. Membr. Sci. **1998**, *139*, 183–200.
17. Rosen, C.; Tragardh, C. Computer Simulations of Mass Transfer in the Concentration Boundary Layer over Ultrafiltration Membranes. J. Membr. Sci. **1993**, *85*, 139–156.
18. Piron, E.; Latrille, E.; Rene, F. Application of Artificial Neural Networks for Crossflow Microfiltration Modeling: Black-Box and Semi-Physical Approaches. Comput. Chem. Engng **1997**, *21* (9), 1021–1030.
19. Bowen, W.R.; Yousef, H.N.S.; Jones, M.G. Prediction of the Rate of Crossflow Membrane Ultrafiltration of Colloids: a Neural Network Approach. Chem. Engng Sci. **1998**, *53* (22), 3793–3802.
20. Niemi, H.; Bulsari, A.; Palosaari, S. Simulation of Membrane Separation by Neural Networks. J. Membr. Sci. **1995**, *102*, 185–191.
21. Foley, G.; Malone, D.M.; MacLoughlin, F. Modeling the Effects of Particle Polydispersity in Crossflow Filtration. J. Membr. Sci. **1995**, *99*, 77–88.
22. Dharmappa, H.B.; Verink, J.; Aim, R.B.; Yamamoto, K.; Vigneswaran, S. A Comprehensive Model for Cross-Flow Filtration Incorporating Polydispersity of the Influent. J. Membr. Sci. **1992**, *65*, 173–185.
23. Niemi, H.; Palosaari, S. Calculation of Permeate Flux and Rejection in Simulation of Ultrafiltration and Reverse Osmosis Processes. J. Membr. Sci. **1993**, *84*, 123–137.
24. Niemi, H.; Palosaari, S. Flowsheet Simulation of Ultrafiltration and Reverse Osmosis Processes. J. Membr. Sci. **1994**, *91*, 111–124.
25. Bird, R.B.; Stewart, W.E.; Lightfoot, E.N. *Transport Phenomena*; John Wiley and Sons: New York, 1960.
26. Backstrom, G. *Fields of Physics on the PC by Finite Element Analysis*; Studentlitteratur: Lund, Sweden, 1994.
27. McCoy, B.J. Membrane Sieving of a Continuous Polydisperse Mixture Through Distributed Pores. Sep. Sci. Technology **1995**, *30* (4), 487–507.
28. Mochizuki, S.; Zydney, A.L. Theoretical Analysis of Pore Size Distribution Effects on Membrane Transport. J. Membr. Sci. **1993**, *82*, 211–227.
29. Wang, Y.X.; Wang, S.C.; Yu, K.T. A Statistic Model of Pore Size Distributions in Membranes. J. Membr. Sci. **1992**, *72*, 13–20.

MARCEL DEKKER, INC.
270 Madison Avenue, New York, New York 10016

30. Zydney, A.L.; Aimar, P.; Meireles, M.; Pimbley, J.M.; Belfort, G. Use of the Lognormal Probability Density Function to Analyze Membrane Pore Size Distributions: Functional Forms and Discrepancies. J. Membr. Sci. **1994**, *91*, 293–298.
31. Nassehi, V. Modeling of Combined Navier–Stokes and Darcy Flows in Crossflow Membrane Filtration. Chem. Engng Sci. **1998**, *53* (6), 1253–1265.
32. Ganguly, S.; Bhattacharya, P.K. Development of Concentration Profile and Prediction of Flux for Ultrafiltration in a Radial Cross-Flow Cell. J. Membr. Sci. **1994**, *97*, 185–198.
33. Kozinski, A.A.; Schmidt, F.P.; Lightfoot, E.N. Velocity Profiles in Porous-Walled Ducts. Ind. Engng Chem. Fundam. **1970**, *9* (3), 502–505.
34. Gupta, B.K.; Levy, E.K. Symmetrical Laminar Channel Flow with Wall Suction. J. Fluids Engng **1976**, *98* (3), 469–474.
35. Berman, A.S. Laminar Flow in Channels with Porous Walls. J. Appl. Phys. **1953**, *24* (9), 1232–1235.
36. Middleman, S. *An Introduction to Fluid Dynamics: Principles of Analysis and Design*; John Wiley and Sons: New York, 1998.
37. Davis, R.H.; Sherwood, J.D. A Similarity Solution for Steady-State Crossflow Microfiltration. Chem. Engng Sci. **1990**, *45* (11), 3203–3209.
38. Vassilieff, C.S. An Elliptic Filtration Variation on Poiseuille-Type Laminar Solutions of Navier–Stokes Equations. J. Membr. Sci. **1994**, *91*, 153–161.
39. PDEase2. SPDE. Inc., Bass Lake, CA, 1995.
40. Munson-McGee, S. H., in preparation.

Received June 2000
Revised October 2000

Request Permission or Order Reprints Instantly!